JOURNAL OF GEOPHYSICAL RESEARCH, VOL. 113, A11221, doi:10.1029/2008JA013593, 2008

A model of the secondary radiation belt

R. S. Selesnick,[1,2] M. D. Looper,[1] and R. A. Mewaldt[3]

Received 8 July 2008; revised 22 September 2008; accepted 30 September 2008; published 29 November 2008.

[1] Products of nuclear reactions between primary radiation belt protons and constituents of the tenuous upper atmosphere form a collocated secondary radiation belt. A calculation of the time-dependent secondary intensity provides a model specification of this environmental component for low- and medium-altitude satellite orbits. It is based on an earlier model of the radiation belt protons, the novel feature being a determination of the secondary source function from nuclear reaction cross sections. All long-lived secondary products are included, isotopes of H and He being dominant while the heavier Li to O isotopes are present at relatively low levels. Secondary protons are shown to be a minor correction to the primary radiation belt.

Citation: Selesnick, R. S., M. D. Looper, and R. A. Mewaldt (2008), A model of the secondary radiation belt, *J. Geophys. Res.*, *113*, A11221, doi:10.1029/2008JA013593.

1. Introduction

[2] The inner radiation belt consists mainly of intense, geomagnetically trapped, energetic protons. They traverse the tenuous upper atmosphere and the resulting nuclear collisions lead to secondary particles that follow similar trajectories to the protons, a significant fraction of which thereby are also trapped and form a secondary radiation belt. Isotopes of trapped hydrogen (^{2}H, ^{3}H) and helium (^{3}He, ^{4}He) have been observed from several low-altitude satellites [*Wefel et al.*, 1995; *Chen et al.*, 1996; *Looper et al.*, 1996, 1998; *Selesnick and Mewaldt*, 1996; *Bakaldin et al.*, 2002; *Bidoli et al.*, 2003; *Leonov et al.*, 2005].

[3] Properties of these trapped particles, such as their relative and absolute intensity levels, energy spectra, and pitch angle distributions, all support their secondary origin, the overabundance of ^{3}He relative to ^{4}He being particularly persuasive. These properties have been predicted by several theoretical calculations that led to substantial agreement with the observations [*Chen et al.*, 1996; *Selesnick and Mewaldt*, 1996; *Pugacheva et al.*, 1998; *Galper et al.*, 2003; *Leonov et al.*, 2008].

[4] The calculations have been of limited scope in accord with the limited data availability. They variously have not included time dependence, radial diffusion, or other details of radiation belt dynamics, nor have they accounted for secondaries heavier than helium. A comprehensive secondary model should overcome all of these limitations and would be of value in specifying the radiation environment for low- to medium-altitude satellite orbits. The construction of such a model is the subject of this paper.

[5] The secondary model is based on our original theoretical model of the radiation belt protons [*Selesnick et al.*, 2007a] (hereinafter referred to as S07). That model forms the primary proton flux from which the secondary source is calculated. Also, many radiation belt processes subsequent to trapping have identical or similar implementations in the two models. The main difference between them is in the source functions. For primary protons the sources are CRAND (cosmic ray albedo neutron decay) and solar protons. The secondary source functions are derived from nuclear reaction cross sections. In the following emphasis is placed on their description, after an outline of the other principal model components. Sample model results are then described.

2. Model Outline

[6] The trapped secondary nuclei satisfy the continuity equation

$$\frac{\partial}{\partial t}\left(\frac{j_i}{v}\right) + \frac{\partial}{\partial E}\left(\frac{dE}{dt}\frac{j_i}{v}\right) = \tilde{S}_i - \frac{j_i}{v\tau_i} \tag{1}$$

where j_i is the intensity of particle species i, which is a function of time t, kinetic energy E (or equivalently speed v), equatorial pitch angle α_0, and L shell. The net source rate $\tilde{S}_i = S_i + S_d + S_s$, where S_i is the secondary source described in the following section. The other model inputs, defined below, are $\frac{dE}{dt}$, S_d, S_s, and τ_i. This section describes in brief those aspects of the model for which details have been presented previously (S07).

[7] The radial diffusion source term S_d is the same as that of the proton model for common trapped particle total kinetic energy. It may be positive or negative, but its main effect is the inward diffusion of solar particles after they are trapped at $L \geq 2$.

[8] The solar injection source S_s is included only for ^{4}He and, as in the proton model, is proportional to the fluence energy spectrum of each solar particle event. The ^{4}He fluence is $F_{He}(E) = F_p(E/2)/40$, determined from shifted

[1]The Aerospace Corporation, Los Angeles, California, USA.
[2]Now at Los Angeles, California, USA.
[3]Physics Department, California Institute of Technology, Pasadena, California, USA.

0148-0227/08/2008JA013593$09.00

solar event energy spectra [*Mewaldt et al.*, 2005, Figure 14], where E is the total ^{4}He kinetic energy and $F_p(E_p)$ is solar proton fluence spectrum for proton kinetic energy E_p. Solar events must also include low abundances of nuclei other than protons and ^{4}He but these are neglected.

[9] The model equation (1) is solved on a grid of the three adiabatic invariants, M, K, and L, and time t. The radial coordinate L is related to the magnetic flux through a drift shell with a fixed proportionality constant, based on the year 2000 geomagnetic dipole moment, so that L remains invariant. The second invariant K is equivalent to the mirror magnetic field or equatorial pitch angle at a fixed time, though not in a varying geomagnetic field. The first invariant M is related to the kinetic energy.

[10] Particle trapping can be long-lived, requiring that the geomagnetic secular variation be taken into account. The presently decreasing dipole moment causes gradual lowering of drift shells into regions of increased atmospheric density and trapped particle heating due to adiabatic compression; between AD 1600 and 1900 the reverse was true: an increasing dipole moment caused rising drift shells and adiabatic cooling. These effects are included via a series of eight geomagnetic field models applicable to fixed epochs from AD 1600 to 2005 (shorter lifetimes relative to the trapped protons preclude the necessity for field models from earlier epochs). Particle rigidity trapping limits and drift averaged atmospheric densities were calculated by numerical trajectory integrations in each field model, with intermediate values obtained by interpolation.

[11] The rate of continuous energy change $\frac{dE}{dt}$ is the total from ionization of the neutral atmosphere and plasmasphere, energy loss to free electrons of the plasmasphere and ionosphere, and adiabatic heating or cooling. Tabulated ionization losses as a function of energy for each trapped particle type are weighted by the drift average densities for each drift shell corresponding to a M, K, and L grid point. (Ionization of the plasmaspheric ions, a minor contributor to the total, has been added since the original proton model by using an additional weighting factor $\frac{Z-q}{Z}$ relative to the neutral atom loss rates, for target plasma ion He and O charge states of $q = 1$ and atomic numbers $Z = 2$ and 8.) Neutral and plasma densities are provided by a model atmosphere and a model plasmasphere respectively, which are each parameterized by the solar radio flux $F_{10.7}$. A history of $F_{10.7}$ thereby provides the model solar cycle dependence.

[12] The lifetime τ_i represents losses by nuclear decay and inelastic scattering, $\tau_i^{-1} = \ln(2)\, t_{1/2}^{-1} + v\sum_k \langle n_k \rangle \sigma_{ik}^I$, where $\langle n_k \rangle$ is the drift averaged nuclear density of atmospheric or plasmaspheric constituent k and σ_{ik}^I is the corresponding parameterized inelastic total cross section [*Tripathi et al.*, 1999]. The only unstable secondaries are ^{3}H, ^{10}Be, and ^{14}C, with respective half-lives of $t_{1/2}$ = 12.32 years, 1.51×10^6 years, and 5700 years. (Neutral ^{7}Be has a 53.22 day half-life for decay by electron capture, but we assume this does not occur in the radiation belt as the trapped particles are fully ionized.)

[13] The solution to equation (1) is

$$j_i(E,t) = v\int_{t_0}^{t} \tilde{S}_i(E',t') e^{-\int_{t'}^{t}\left(\frac{\partial \frac{dE}{dt}}{\partial E''\, dt} + \frac{1}{\tau_i}\right) dt''} dt' \qquad (2)$$

where $\frac{dE}{dt}$ and τ_i are each evaluated at E'' and t'', and where E' or E'' is the energy at time t' or t'', respectively. The initial condition is $j = 0$ at $t' = t_0$, which is the time when E' is equal to the maximum trapped particle energy or trapping limit. The solution at a given time t requires the source function be evaluated at all prior times from t_0 to t. The energy E' as a function of time t' is obtained by integrating $\frac{dE}{dt}$. The secondary source also requires the primary proton intensity at all prior times, as described below, which was obtained by running the proton model for all times back to AD 1600.

3. Secondary Source

[14] The local source rate for secondary particles of type i from nuclear reactions between primary incident protons with intensity j_p and target nuclei of all types k with nuclear densities n_k is

$$S_i(E,\alpha,t) = \sum_k \int dE_p \int d\Omega_p j_p(E_p,\alpha_p,t) n_k(t) \frac{d^2\sigma_{ik}}{dE d\Omega}(E_p,E,\theta) \qquad (3)$$

where σ_{ik} is the cross section for producing a single secondary particle. The integrals cover all incident proton energies E_p and local pitch angles α_p, included in solid angle Ω_p, that lead to a given secondary energy E and local pitch angle α. The double differential cross section is evaluated at E_p and E, and at the scattering angle θ between the primary and secondary directions obtained geometrically:

$$\cos\theta = \cos\phi \sin\alpha_p \sin\alpha + \cos\alpha_p \cos\alpha \qquad (4)$$

where ϕ is the difference between the primary and secondary gyrophase angles.

[15] The secondary intensity j_i is assumed to be independent of the distance s along any trapped particle trajectory. This allows the model equation (1) to be averaged over s, or drift averaged, which is done by integrating along the spiral path of the trapped secondary for several drift orbits and then dividing by the total path length s_T: $\langle \ldots \rangle \equiv \frac{1}{s_T}\int \ldots ds$. The model j_p is a function of M, K, L, and time, but the drift averages are computed at a fixed time so M and K are equivalent to E and B_m. The source rate should be computed as a function of these variables. Therefore it is convenient to change variables from α and α_p to the equivalent mirror magnetic field magnitudes B_m and B_{mp}, to which they are related by conservation of M:

$$B_m \sin^2\alpha = B_{mp}\sin^2\alpha_p = B \qquad (5)$$

where B is the guiding center magnetic field at a given s, rather than the local field, because of the large gyroradius at high energies. Substituting this and $d\Omega_p = \sin\alpha_p d\alpha_p d\phi$ into equation (3) and drift averaging,

$$S_i(E,B_m) = \int dE_p \int dB_{mp} j_p(E_p,B_{mp}) Q_i(E,B_m,E_p,B_{mp}) \qquad (6)$$

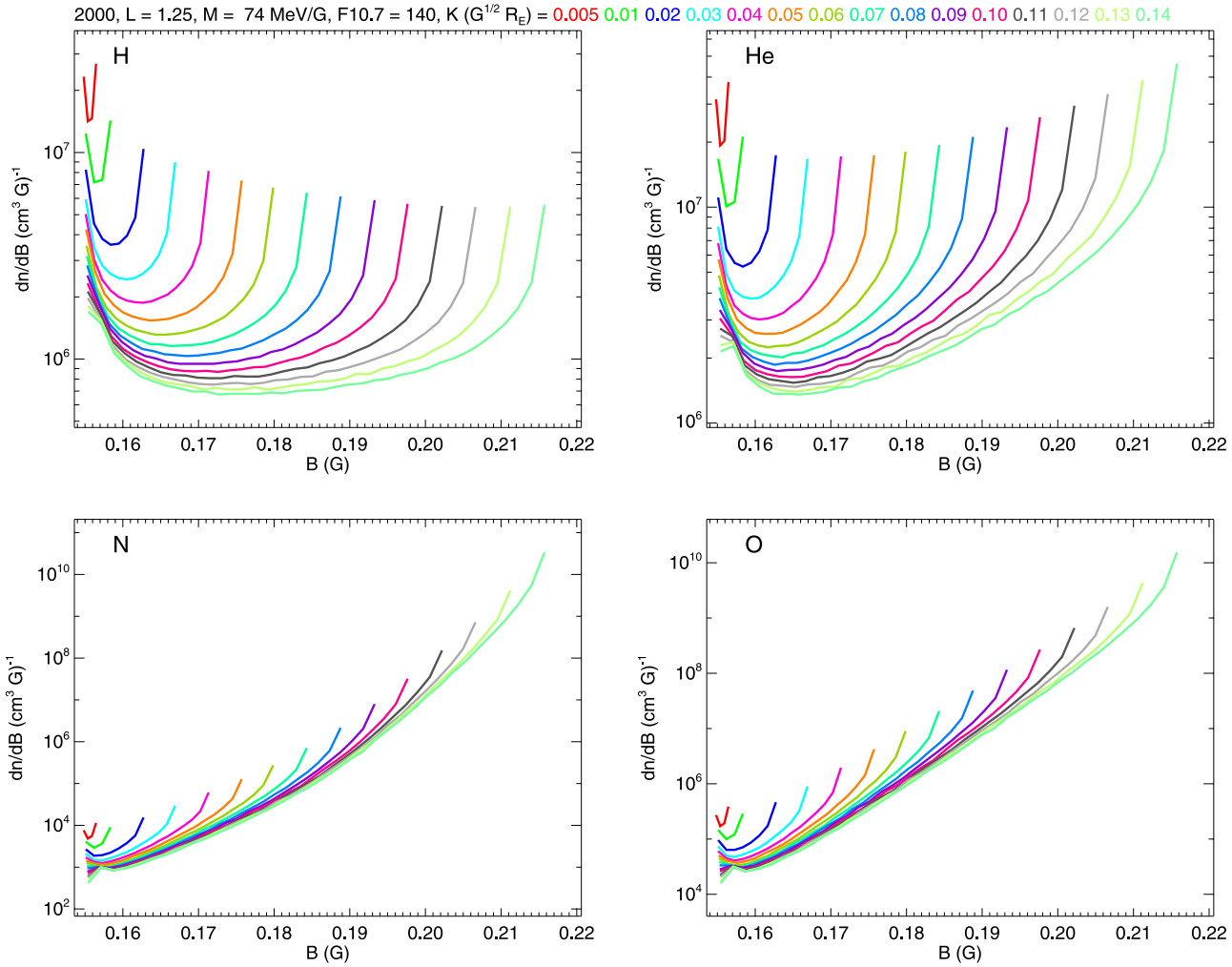

Figure 1. Magnetic field derivatives of drift averaged nuclear densities for each of the four major atmospheric constituents versus B in year 2000 for selected M, K, and L values.

where

$$Q_i(E, B_m, E_p, B_{mp}) = \left\langle g(B, B_{mp}) \sum_k n_k(s) \int_0^{2\pi} d\phi \frac{d^2\sigma_{ik}}{dEd\Omega} \right\rangle \quad (7)$$

and

$$g(B, B_m) = \frac{B}{2B_m^2} \left(1 - \frac{B}{B_m}\right)^{-\frac{1}{2}} \quad (8)$$

Equation (5) does not determine the signs of $\cos\alpha$ and $\cos\alpha_p$, but θ from equation (4) depends on whether they are the same or opposite. Therefore both possibilities must be included in the drift averages.

[16] Now the drift averages can be precomputed as a function of E, B_m, E_p, and B_{mp}, parameterized by $F_{10.7}$ and for each magnetic field model but independently of j_p. This is a significant benefit because the time dependence of j_p requires computation of S_i at each time step, which would be prohibitive if the drift averaging were included.

[17] In the drift average only n_k is an explicit function of s while g and σ_{ik} are functions of s only through B. Therefore a further simplification is made by changing the integration variable from s to B:

$$Q(E, B_m, E_p, B_{mp}) = \int dB\, g(B, B_{mp}) \sum_k \frac{dn_k}{dB} \int_0^{2\pi} d\phi \frac{d^2\sigma_{ik}}{dEd\Omega} \quad (9)$$

where

$$\frac{dn_k}{dB} \equiv \frac{1}{s_T} \sum_j n_k(s_j) \frac{ds}{dB} \approx \frac{1}{s_T \delta B} \int_{B \in \delta B} n_k(s) ds \quad (10)$$

which includes a sum of the n_k values from all of the locations s_j where the trajectory passes through a given B during the entire drift average. The last approximation shows how $\frac{dn_k}{dB}$ is computed numerically by drift averaging only the n values for which B is contained within the small range δB. This allows the drift averaging to be done independently of σ_{ik} as well as j_p.

[18] Sample curves of $\frac{dn_k}{dB}$ versus B for each target element, H, He, N, and O, are shown in Figure 1. The variation between the results for each element is caused by their

altitude distributions, with O and N concentrated at lower altitudes than H and He. The individual curves are peaked at $B = B_m$ due to the long path length near the mirror points, and at the equatorial (minimum) B due to the small change in B near its minimum for a given path length. The g factor in equation (9) adds additional weighting near the mirror points. The drift averaging method described above is more accurate than earlier calculations based on the simplifying assumption that interactions occur at the equator [*Selesnick and Mewaldt*, 1996], as recently highlighted [*Galper et al.*, 2003; *Leonov et al.*, 2008].

4. Cross Sections

[19] Production cross sections for the impact of energetic protons on atmospheric constituents were primarily determined by a Monte Carlo simulation of the nuclear reactions using the software toolkit Geant4 (version 9.1.p01 with the QGSP_BERT physics list, running on a FreeBSD 6.2 cluster with gcc 3.4.6) [*Agostinelli et al.*, 2003]. (A similar implementation was used to simulate neutron albedo for the proton model (S07).) In this simulation 6.45×10^{10} protons at each of 25 approximately logarithmically spaced energies from 4 to 4000 MeV entered a rectangular box of gaseous H_2, He, N_2, or O_2. The dimensions of the box were varied with proton energy and target material so as to minimize ionization energy loss of the product particles in the target while still accumulating $\sim 10^5$ to 10^7 nuclear interactions. The species, energy, and direction of each ion or nucleon leaving the simulation volume were tabulated, excluding the primary beam.

[20] Cross sections were calculated from the simulation results in the center-of-mass (CM) reference frame. Secondary products of type i, from protons with energy E_p in the model (or LAB) reference frame incident on target k, were binned by secondary CM energy E^c and scattering angle θ^c. (Quantities with superscript c are in the CM frame and without it are in the LAB frame.) For N_{iklm} secondaries in energy bin l of width ΔE_l^c and angle bin m of solid angle $\Delta\Omega_m^c$,

$$\frac{d^2\sigma_{ik}}{dE^c d\Omega^c} = \frac{N_{iklm}}{N_p n_k L \Delta E_l^c \Delta\Omega_m^c} \tag{11}$$

where N_p is the number of protons incident on a target of density n_k and thickness L.

[21] The highest E^c bin is centered on the CM energy of 2-body elastic scattering or 2-body reactions:

$$E_N^c = \frac{\epsilon^2 + m_i^2 - m_r^2}{2\epsilon} \tag{12}$$

where $\epsilon = \sqrt{2E_p m_t + m_p^2 + m_t^2}$ is the total CM energy, m_i is the secondary mass, m_p is the proton mass, m_t is the target nuclear mass, and m_r is the mass of the remaining scattered particle (in this section the speed of light $\equiv 1$). For example, secondary ^{3}He from protons incident on ^{4}He would require m_r to be the mass of ^{2}H. There are $N = 16$ bins spaced logarithmically in kinetic energy covering four decades below $E_N^c - m_i$.

[22] Some results of the Geant4 simulation were clearly deficient and we have supplemented them with experimental data in the highest E^c bin: for elastic scattering of protons on all targets the Geant4 simulation underestimated the cross sections for $E_p \leq 15$ MeV and these have been replaced with results obtained from the EXFOR database [http://www-nds.iaea.org/exfor/exfor00.htm]; the reaction $p + p \rightarrow {}^2H + \pi^+$ was not represented in the simulation and was added for $300 < E_p < 3000$ MeV [*Ramaty and Lingenfelter*, 1969] assuming an isotropic secondary distribution, which is valid near the reaction threshold [*Drochner et al.*, 1998], and the reaction $p + {}^4He \rightarrow {}^2H + {}^3He$, also not represented, was added for $40 < E_p < 400$ MeV [*Selesnick and Mewaldt*, 1996]. In the cases of secondary ^{6}Li, ^{7}Li, and ^{7}Be the Geant4 results led to total cross sections that were significantly lower than experimental data [*Moskalenko and Mashnik*, 2003], but they were used without supplementation because differential cross section data were not available; it is likely that the missing secondaries would be at low enough energy (in the LAB frame) so as not to contribute to the radiation belt model. Some sample cross sections from the Geant4 simulation and supplementary data are shown in Figure 2.

[23] The model calculation requires cross sections in the LAB frame. To simplify the integration over ϕ (see below) these are approximated as a sum over the E^c bins:

$$\frac{d^2\sigma_{ik}}{dE d\Omega} \approx \sum_{l=1}^{N} \frac{d\sigma_{ik}}{dE} \frac{\delta(\theta - \theta_l)}{2\pi \sin\theta} \tag{13}$$

(This is the same level of approximation as was introduced by binning the Geant4 results.) The single differential cross sections are related by

$$\frac{d\sigma_{ik}}{dE} = \frac{2\pi}{\gamma\beta p^c} \frac{d\sigma_{ik}}{d\Omega^c} \approx \frac{2\pi}{\gamma\beta p^c} \frac{d^2\sigma_{ik}}{dE^c d\Omega^c} \Delta E_l^c \tag{14}$$

obtained from the CM to LAB transformation with Lorentz factor $\gamma = \frac{E_p + m_t}{\epsilon}$ and corresponding speed β, and where p^c is the CM secondary momentum. The CM and LAB scattering angles are related by

$$\tan\theta = \frac{\sin\theta^c}{\gamma\left(\cos\theta^c + \frac{\beta}{\beta_i^c}\right)} \tag{15}$$

where β_i^c is the CM secondary speed and the CM scattering angle is also obtained from the Lorentz transformation:

$$\cos\theta^c = \frac{E - \gamma E^c}{\gamma\beta p^c} \tag{16}$$

[24] The integral over ϕ from equation (9) is now simplified using equation (13):

$$\int_0^{2\pi} d\phi \frac{d^2\sigma_{ik}}{dE d\Omega} = \frac{1}{\pi} \sum_{l=1}^{N} \frac{d\phi}{d\cos\theta} \frac{d\sigma_{ik}}{dE} \tag{17}$$

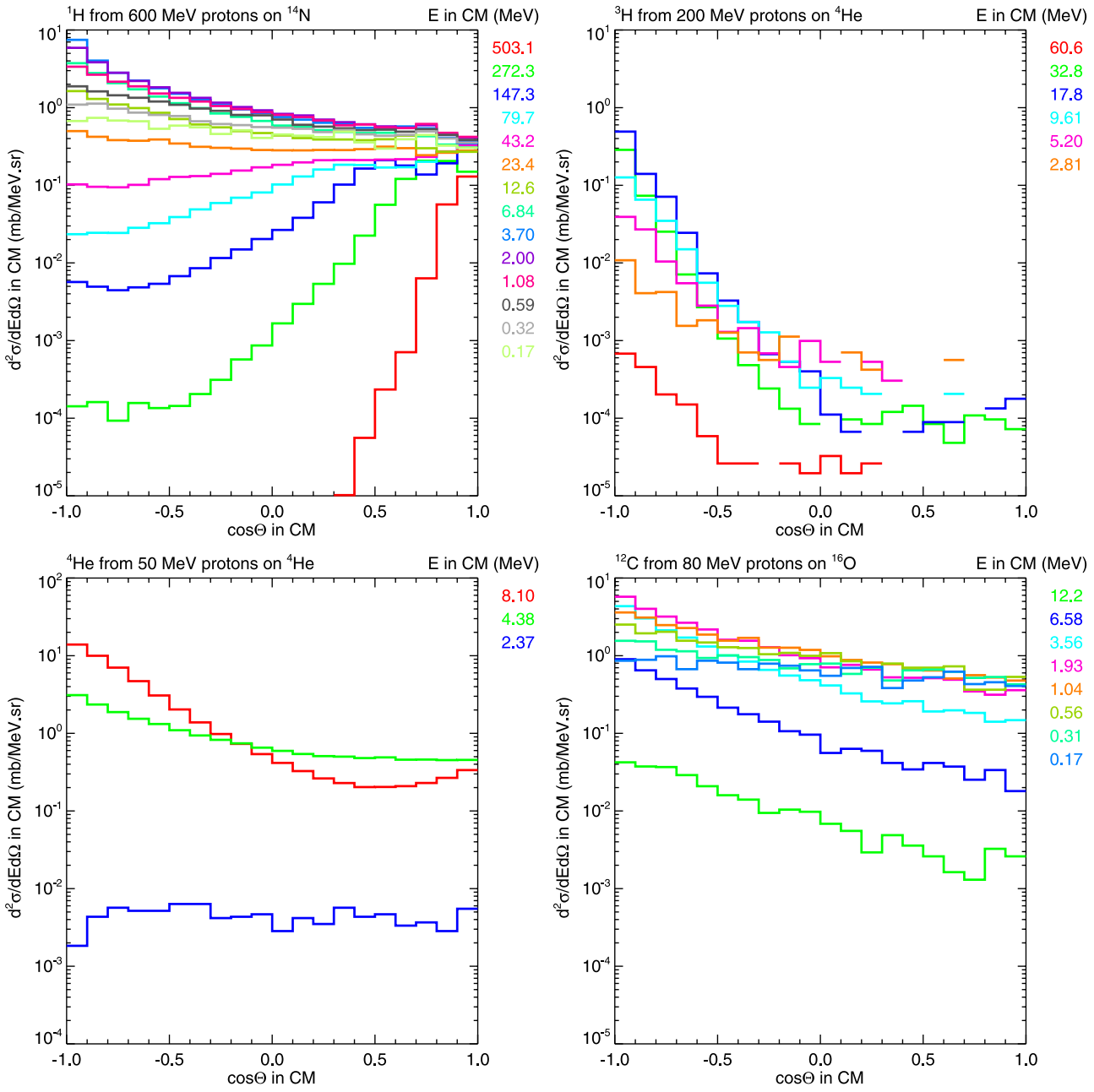

Figure 2. Sample double differential cross sections versus scattering angle cosine in the CM frame. The secondary nucleus, incident proton kinetic energy in the LAB frame, and target nucleus are listed above, and the secondary CM kinetic energies are listed to the right of each plot.

where symmetry about $\phi = \pi$ has introduced a factor 2 and, from equation (4),

$$\frac{d\phi}{d\cos\theta} = \frac{1}{\sin\phi \sin\alpha_p \sin\alpha} \tag{18}$$

The terms in the summation of equation (17) are evaluated at the secondary energies E_l, modified by adjusting the upper limit of equation (12) for a given E_p, and the corresponding scattering angles θ_l from equations (15) and (16), with the cross sections interpolated from the discrete E_p and θ_1 values at each l. Pure elastic scattering and 2-body reactions are included as the Nth term in the summation.

5. Secondary Protons

[25] Primary and secondary protons are indistinguishable. The proton model should therefore include a combined source of primary CRAND and solar protons and secondary scattered protons, and combined losses from inelastic and elastic scattering. The original proton model neglected the

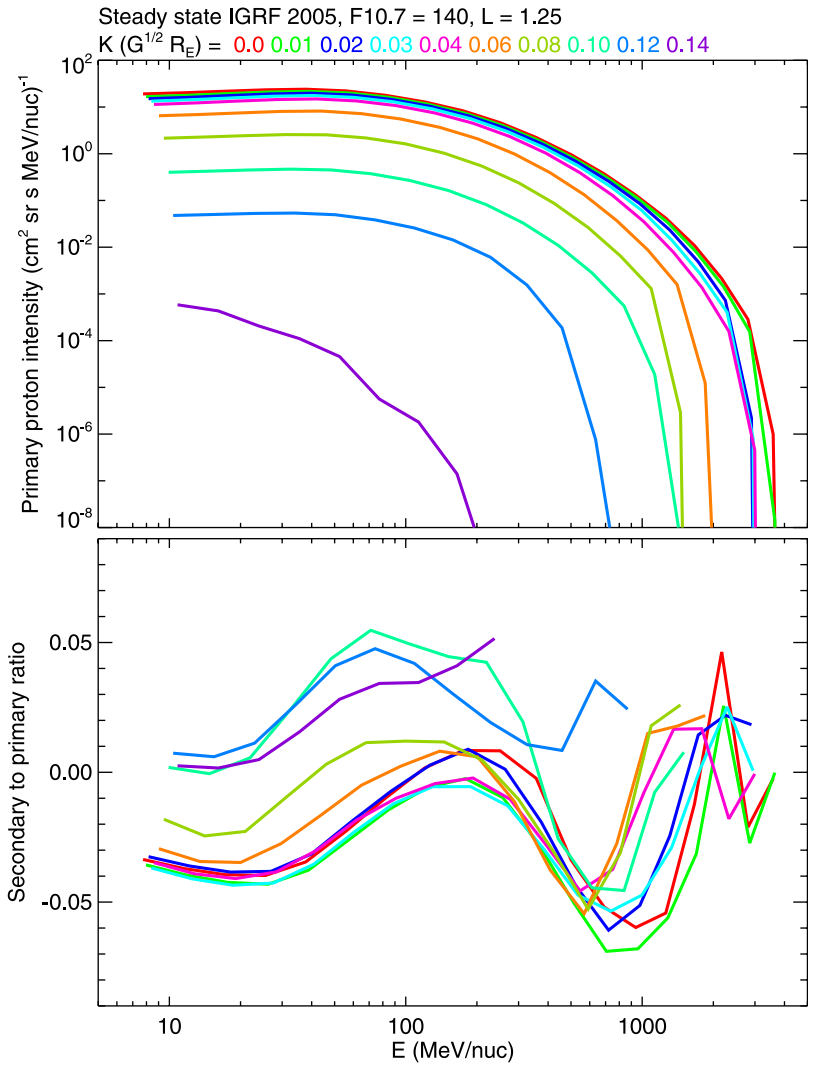

Figure 3. (top) Primary proton energy spectra for selected K values at $L = 1.25$ from the steady state model. (bottom) Ratio of secondary to primary protons. The secondaries are from elastic and inelastic nuclear scattering and are balanced by elastic scattering losses of primary protons; thus the secondary intensity may be negative.

secondary source and elastic scattering losses. To justify this we consider a model proton intensity $j_p = j + \delta j$, where j is the original primary model solution and δj is the secondary proton model. For simplicity we assume, in this section only, a steady state at $L = 1.25$ with only the CRAND primary source and no diffusion.

[26] The primary model is

$$\frac{\partial}{\partial E}\left(\frac{dE}{dt}\frac{j}{v}\right) = S_c - \frac{j}{v\tau_i} \tag{19}$$

where S_c is the CRAND source rate and τ_i is the inelastic scattering lifetime. Subtracting this from the combined equation for j_p leaves the secondary model

$$\frac{\partial}{\partial E}\left(\frac{dE}{dt}\frac{\delta j}{v}\right) = S_i - \frac{j}{v\tau_e} - \frac{\delta j}{v\tau_i} \tag{20}$$

where S_i is the secondary proton source, τ_e is the elastic scattering lifetime, and elastic scattering of secondary protons has been neglected.

[27] The solutions of equations (19) and (20) are similar:

$$j(E) = \frac{-v}{\frac{dE}{dt}}\int_E^{E_L} S_c(E')e^{\int_E^{E'}\frac{dE''}{\tau_i(E'')\frac{dE}{dt}(E'')}}dE' \tag{21}$$

$$\delta j(E) = \frac{-v}{\frac{dE}{dt}}\int_E^{E_L}\left[S_i(E') - \frac{j}{v\tau_e}\right]e^{\int_E^{E'}\frac{dE''}{\tau_i(E'')\frac{dE}{dt}(E'')}}dE' \tag{22}$$

where E_L is the energy at the trapping limit. They are illustrated in Figure 3, with j above and $\frac{\delta j}{j}$ below. They show that $|\delta j| \lesssim 0.07j$ in this case. The elastic scattering source and loss are of similar magnitude and dominate the inelastic source. The generally negative δj at low K and positive δj at high K show the diffusive nature of the scattering, as the intensity gradient in K is reduced. The smallness of $|\delta j|$ justifies our neglecting it and only the primary proton

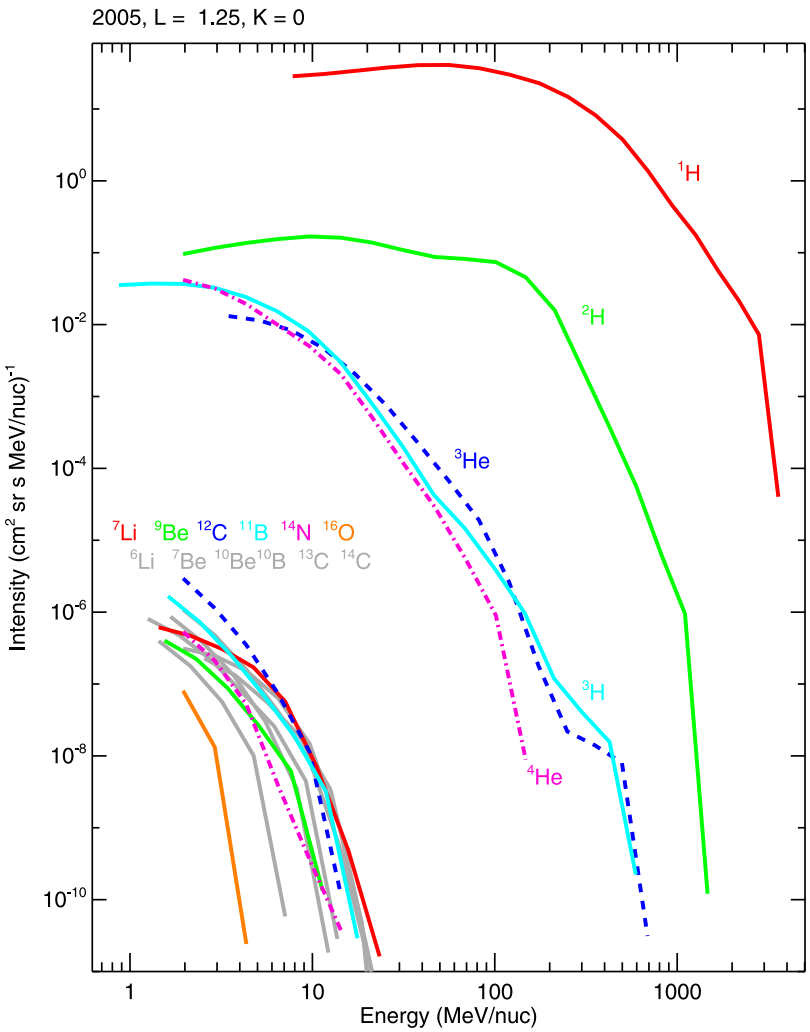

Figure 4. Model equatorial energy spectra of all trapped secondaries and of primary protons for L = 1.25 and year 2005.

intensity $j_p = j$ is applied to the secondary model. (Similar conclusions have been reached previously [*Dragt*, 1971].)

6. Model Results

[28] The model has been run for all long-lived secondary products of protons incident on atmospheric H, He, N, and O, and on plasmaspheric H^+, He^+, and O^+, providing their intensity as functions of M, K, L in the range 1.1 to 2.4, and time during the years 1969 to 2005 (~3 solar cycles). Some of the results are described below.

[29] Sample energy spectra for all of the secondaries at L = 1.25 and at the magnetic equator (K = 0) in 2005 are shown in Figure 4. The primary proton model spectrum is also included for comparison. The lower energy limits of the spectra correspond to the lowest model M value of 50 MeV/G. They could, in principle, be extended to lower energies, though they may be influenced there by unmodeled processes such as charge exchange. The upper energy limits are not at the highest model M value, but rather are the highest energies at which each secondary can kinematically be produced by the local trapped proton distribution. For this reason the secondary spectra generally do not extend up to their local trapping limits, as do the trapped proton spectra (S07). The differences between the trapping limits and spectral upper limits are negligibly small for the isotopes of H but are significant for the heavier secondaries. For example, the estimated trapping limit for both ^{2}H and ^{4}He in Figure 4 is ~1800 MeV/nucleon (S07), which is near the ^{2}H spectral upper limit but well above the ^{4}He spectral upper limit of 150 MeV/nucleon.

[30] At a given kinetic energy per nucleon the secondary H and He isotopes, which are produced primarily from atmospheric He, have significantly higher intensity than the heavier secondaries produced from N and O. This is due in part to the greater scale height of atmospheric He, but primarily to the differing energy and angle dependences of the production cross sections. Secondaries from atmospheric N and O by direct, or knockout, reactions are produced at comparably high energies to those from He. If these were the prevalent reactions then the secondary intensity at these energies would also be comparable, but instead the intra-nuclear cascade reactions are dominant and, due to dissipation of the primary energy among multiple secondaries, the resulting secondary energies are mostly too low to be included in our results. Thus a detailed

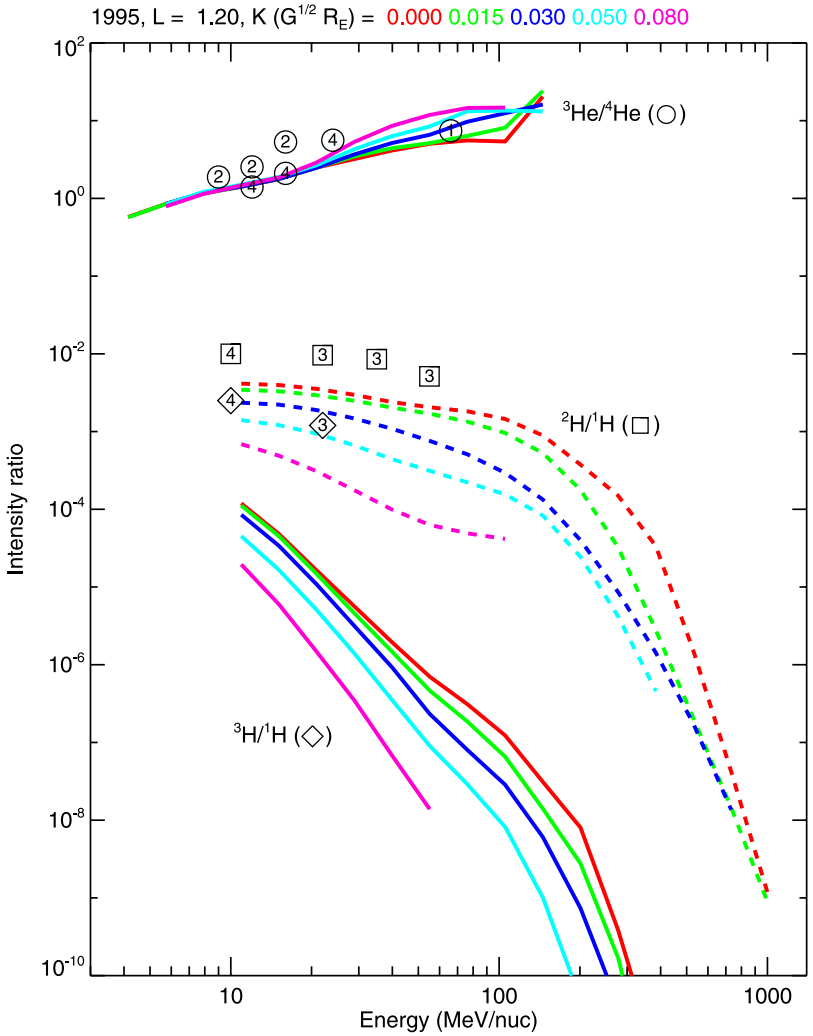

Figure 5. Model intensity ratios ^{3}He/^{4}He (upper solid curves), ^{2}H/^{1}H (dashed curves), and ^{3}H/^{1}H (lower solid curves) at common energy per nucleon for selected K values with $L = 1.2$ in 1995. Numbered symbols represent observations by: 1, the ONR-64 instrument on the CRRES satellite [*Chen et al.*, 1996] 2, MAST on SAMPEX [*Selesnick and Mewaldt*, 1996]; 3, PET on SAMPEX [*Looper et al.*, 1996, 1998]; and 4, NINA on Resurs-01-N4 [*Bakaldin et al.*, 2002].

knowledge of the double differential cross sections is essential to the accuracy of the results. The secondary ^{2}H spectrum at $E \gtrsim 50$ MeV/nucleon is dominated by production from atmospheric H but is uncertain there because of sparse cross section data (see above), and similarly for the spectra of secondary ^{6}Li, ^{7}Li, and ^{7}Be. The lowest-intensity spectrum is that of secondary ^{16}O, which is formed only from scattering of atmospheric or plasmaspheric O.

[31] Model intensity ratios for the H and He isotopes at $L = 1.2$ in 1995 are shown in Figure 5. The ^{1}H intensity is from the primary proton model. The ratios vary with energy and K as shown, but also with L and time due to the changing atmospheric composition. Also shown in the figure for comparison are measurements of the same ratios from various satellites. The satellite data generally cover a range of values in time, energy, L, and K (or equatorial pitch angle, the particle telescopes providing some directionality). With steep intensity gradients direct comparisons with the model can be problematic (see further discussion of this point in the following section). However, large disparities must be significant; the measured ^{3}H/^{1}H ratios are $\gtrsim$20 times the model predictions for reasons that remain unclear [*Bakaldin et al.*, 2002]. Similar results were obtained in two independent measurements so it is likely that the model ^{3}H intensity is too low.

[32] Some examples of the model trapped ^{4}He intensity as a function of time at fixed values of M, K, and L are shown in Figure 6. The fixed M value is the lowest of the model and corresponds to a kinetic energy of ~2 MeV/nucleon at $L = 1.25$ and $K = 0$ in 2005 (Figure 4). The general decrease of the intensity with time at low L and high K is caused by the decreasing geomagnetic dipole moment, which lowers the drift shells into regions of higher atmospheric density (S07).

[33] The ~11 year solar cycle periodicity is particularly evident for K values with corresponding mirror point altitudes (~500 to 1000 km) where the atmosphere also has a substantial periodicity, and for which the trapping lifetimes are not much longer than 11 years. However, the solar cycle dependence is complex: note that the oscillations

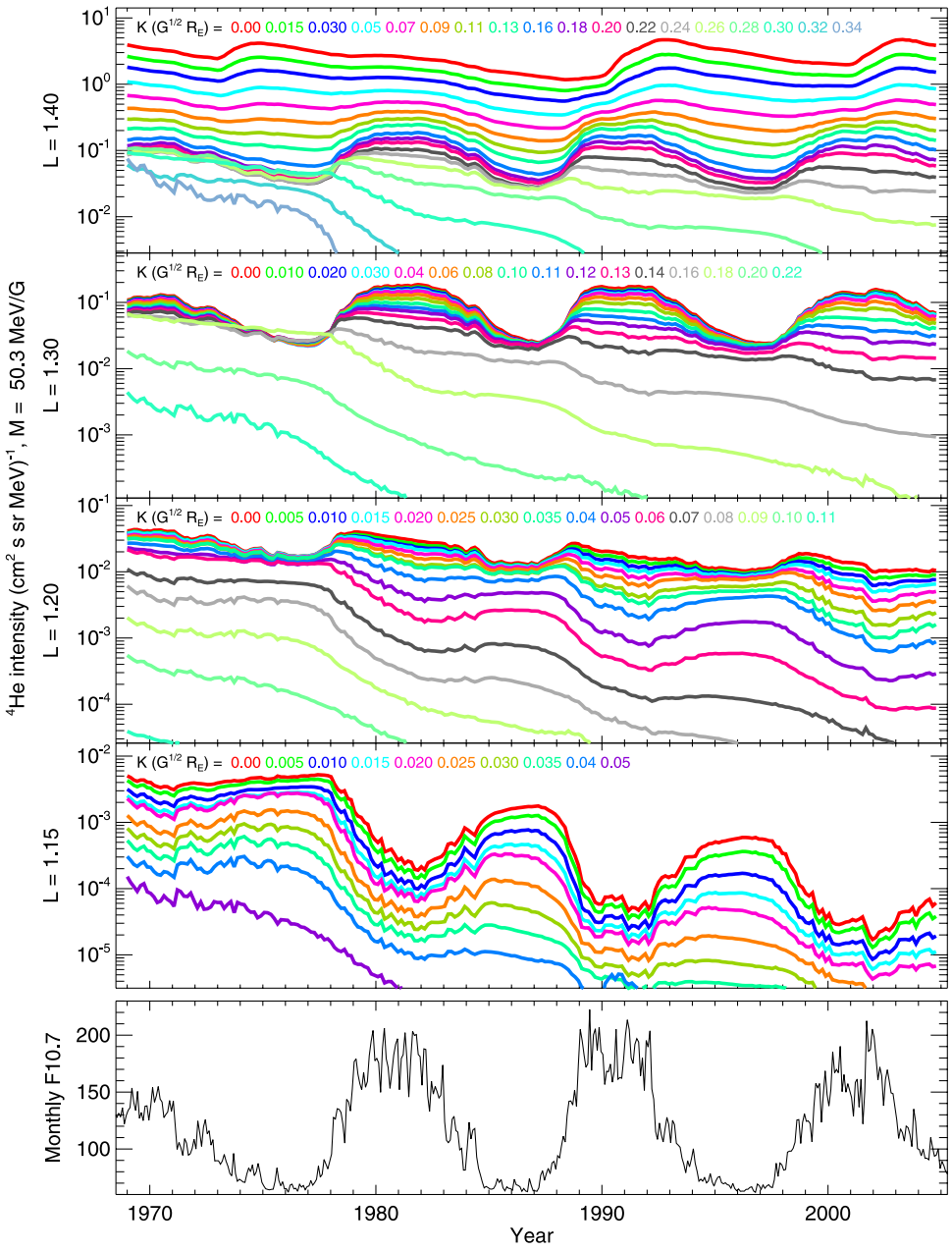

Figure 6. Model trapped ^{4}He intensity versus time in years for selected L, K, and M values. Monthly averages of the solar $F_{10.7}$ radio flux are shown below.

at L = 1.15 and 1.30 are out of phase. This is because of competition between the increased source rate due to the higher atmospheric densities at solar maximum, which wins at higher altitude, and the similarly increased loss rate, which wins at lower altitude. Higher primary proton intensity at low altitude ($\lesssim$1000 km) during solar minimum, as shown by the model (S07) and by observations [*Looper et al.*, 1996], is also a factor.

[34] At L = 1.4 the ^{4}He of solar origin is seen at low K while that of secondary origin, with its solar cycle dependence, is seen at high K. This is because the low K lifetimes are relatively long, allowing time for slow inward diffusion of ^{4}He that was injected at $L > 2$ during solar particle events. Three intensity maxima at L = 1.4 and low K values follow large solar events during 1972, 1989, and 2000 to 2001, with ~3 year delay. They did not reach L = 1.3 because of the slower diffusion rate and shorter lifetimes at lower L. Observed overabundances of ^{4}He relative to the expected secondary component for $L \gtrsim 1.5$ were interpreted as possibly of solar origin [*Selesnick and Mewaldt*, 1996] (the low-altitude orbit of the SAMPEX satellite did not provide access to the lowest K values).

[35] Sample model equatorial pitch angle distributions for ^{2}H, ^{3}He, ^{4}He, and ^{14}C at L values of 1.3 to 1.8 and at fixed energy values during year 2000, obtained by interpolating between the model results at fixed M, are shown in Figure 7. They are relatively flat for the light secondary nuclei at pitch angles outside the atmospheric loss cone. In contrast, the

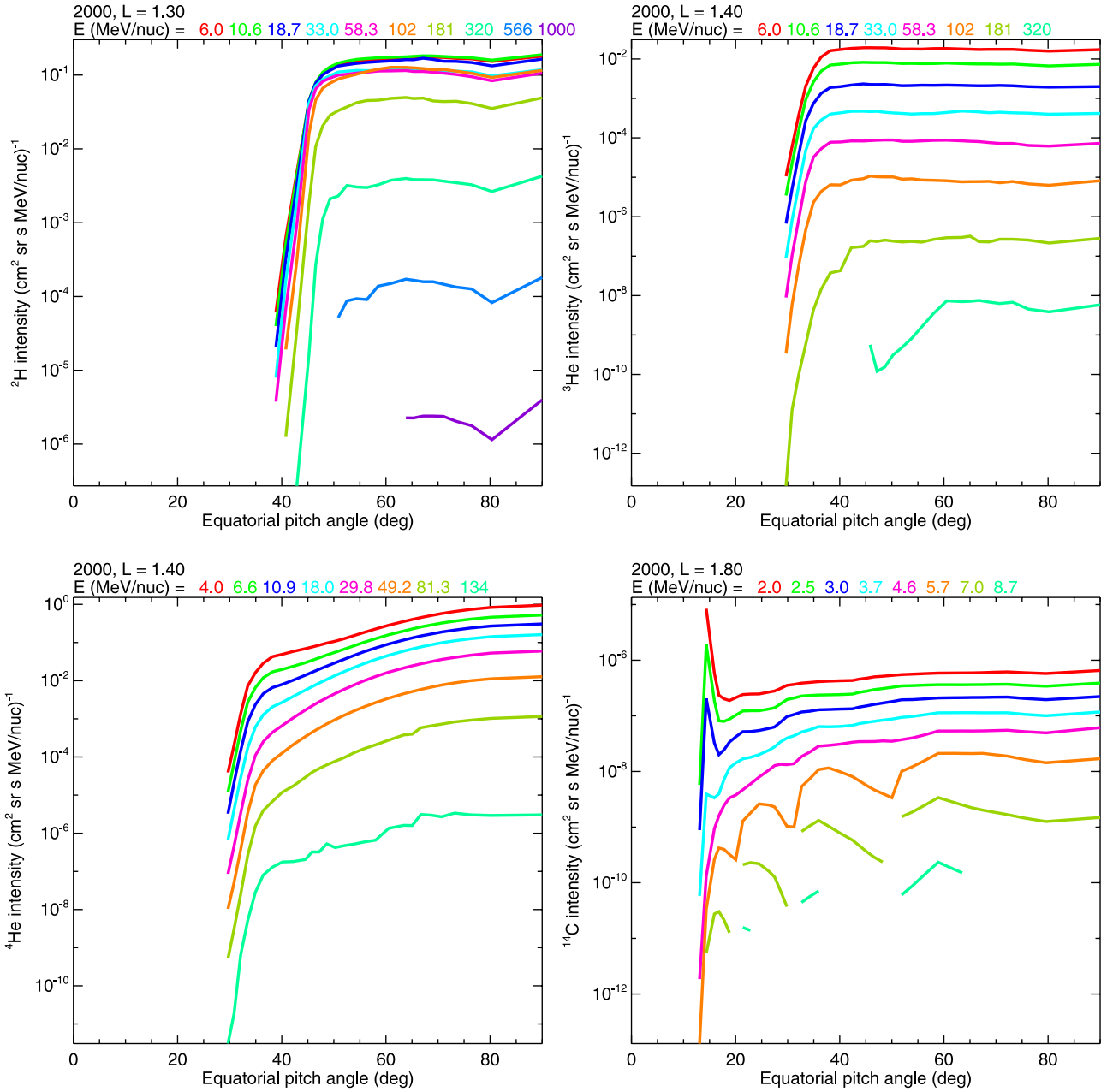

Figure 7. Model equatorial pitch angle distributions, interpolated to selected kinetic energies at selected L values.

solar ^{4}He intensity peaks at 90° as a result of the assumed isotropic solar particle injection combined with higher loss rates at lower K. The low energy ^{14}C distribution shows a sharp peak near the loss cone angle as a result of the concentration of atmospheric N and O at low altitude. The peak does not extend to high energy because of kinematic constraints, manifested in a lack of solutions to equation (16) for θ^c or equation (4) for ϕ, which also explain the presence of dips or gaps in most of the high energy distributions.

7. Discussion

[36] The secondary radiation belt model described above and its parent proton model form a basis for specifying the radiation environment of low- and medium-altitude satellite orbits. They include all major contributing factors thought to determine the intensity of radiation belt H and He isotopes. Isotopes of heavier secondary elements, from Li to O, are also included but have relatively low radiation belt intensity. An additional source of heavy elements, trapping of anomalous cosmic rays, provides significantly greater intensity for N, O, Ne, and possibly C, in the range $L \sim 1.5$ to 2.5 [*Selesnick et al.*, 1995]; empirical and theoretical models of this population are also available [*Selesnick*, 2001]. Trapping of heavy elements from solar particle events may also be significant for $L \gtrsim 1.4$ [*Lorentzen et al.*, 2002; *Mazur et al.*, 2006].

[37] The model results demonstrate the practicality of the methods we have adopted for calculating radiation belt particle intensities from theoretical and empirical inputs. Satellite observations of trapped H and He isotopes provide some tests of the results at kinetic energies ~10 to 50 MeV/nucleon and primarily at low altitudes (such as from the CRRES and SAMPEX satellites and the NINA instruments, see Figure 5). Heavier elements, Li-B, N, and Ar, observed at low intensity for $L < 1.5$ (from the TSUBASA satellite) are likely of secondary origin [*Hareyama et al.*, 2007]. More detailed comparisons with these data sets are possible (see below), while active and future experiments (such as PAMELA [*Picozza et al.*, 2007], AMS [*Gentile*, 2003], and on the planned RBSP [*Sibeck et al.*, 2006]) are expected to provide data at higher energy and altitude, and possibly also for the heavier secondary elements.

[38] The accuracy of the secondary model is dependent in part on the accuracy of the primary proton model. That model compares favorably with the empirical AP-8 model for $L < 1.8$ and with low-altitude satellite data, but is expected to overestimate the proton intensity for $L \gtrsim 1.8$ because observed but unexplained losses during magnetic storms have not been included in the model (S07). Similar expectations should apply to the secondary model.

[39] Most of the radiation belt particles from $L < 2$ are lost to the atmosphere, the rate of outward radial diffusion being small. Their ultimate fates may be of interest in various applications. For example, atmospheric ^{14}C, used in radiocarbon dating, forms in cosmic ray interactions with the upper atmosphere, but the significance of a contribution from the radiation belt source is unknown, and similarly for ^{10}Be obtained from polar ice cores and used to study solar activity and cosmic ray modulation [*Solanki et al.*, 2004]. High ^{7}Be concentrations in the upper atmosphere have been attributed to cosmic ray and solar particle interactions [*Phillips et al.*, 2001], while a secondary radiation belt source has again not been considered. Radiation belt trapping of the secondary particles is not required for them to contribute to atmospheric concentrations, which are therefore determined by the source functions averaged over all secondary directions. The radiation belt, cosmic ray, and solar particle sources of atmospheric secondaries should have different latitude and altitude distributions, which might make it possible to separately identify their contributions. Cosmic rays and solar particles are not a significant source of radiation belt secondaries because their intensities are much lower in the radiation belt than that of the trapped primary protons.

[40] The secondary radiation belt model can be improved in several areas, such as a more accurate primary proton model, improved nuclear physics calculations of the reaction cross sections, or a more detailed parameterization of the atmospheric time dependence. Further improvement can be achieved by data assimilation, particularly when more satellite data sets become available. The first assimilation step is accurate comparison of the model results with satellite data, which can be a fairly involved procedure [*Selesnick et al.*, 2007b]. The model intensity must be converted from the M, K, and L grid to the satellite coordinate system, after which details of instrumental response functions must be applied. Then simulated data points may be constructed to cover the same ranges of energy, pitch angle, and time as the measured data points (such as those in Figure 5). Similar techniques would predict the model radiation environment for orbits of interest in satellite design.

[41] **Acknowledgments.** The work at Aerospace was supported by NSF grant ATM-0518190 under the National Space Weather Program. The work at Caltech was supported by NASA grants NNG04GB55G and NAG5-12929.

[42] Zuyin Pu thanks Reiner Friedel and Xinlin Li for their assistance in evaluating this paper.

References

Agostinelli, S., et al. (2003), Geant4—A simulation toolkit, *Nucl. Instrum. Methods NIM A*, *506*, 250–303, doi:101016/S0168-9002(03)01368-8.

Bakaldin, A., et al. (2002), Geomagnetically trapped light isotopes observed with the detector NINA, *J. Geophys. Res.*, *107*(A8), 1171, doi:10.1029/2001JA900172.

Bidoli, V., et al. (2003), Isotope composition of secondary hydrogen and helium above the atmosphere measured by the instruments NINA and NINA-2, *J. Geophys. Res.*, *108*(A5), 1211, doi:10.1029/2002JA009684.

Chen, J., T. G. Guzik, J. P. Wefel, K. R. Pyle, and J. F. Cooper (1996), Energetic helium isotopes trapped in the magnetosphere, *J. Geophys. Res.*, *101*(A11), 24,787–24,799.

Dragt, A. J. (1971), Solar cycle modulation of the radiation belt proton flux, *J. Geophys. Res.*, *76*(10), 2313–2344.

Drochner, M., et al. (1998), The $p + p \rightarrow \pi^+ + d$ reaction close to threshold at COSY, *Nucl. Phys. A*, *643*, 55–82.

Galper, A. M., S. V. Koldashov, A. A. Leonov, and V. V. Mikhailov (2003), Inner Radiation Belt Generation of Light Nuclei Isotope, *Proc. 28th Int. Cosmic Ray Conf.*, *4*, 4257–4260.

Gentile, S. (2003), The Alpha Magnetic Spectrometer on the International Space Station, *Proc. 28th Int. Cosmic Ray Conf.*, 2145–2148.

Hareyama, M., N. Hasebe, S. Kodaira, N. Masuyama, S. Ota, K. Sakurai, T. Goka, H. Koshiishi, and H. Matsumoto (2007), Charge and mass composition of heavy ions in the Earth's radiation belt, *Proc. 30th Int. Cosmic Ray Conf.*

Leonov, A., et al. (2005), Pitch angle distribution of trapped energetic protons and helium isotope nuclei measured along the Resurs-01 No. 4 LEO satellite, *Ann. Geophys.*, *23*, 2983–2987.

Leonov, A. A., A. M. Galper, S. V. Koldashov, V. V. Mikhailov, M. Casolino, P. Picozza, and R. Sparvoli (2008), Inner radiation belt source of helium and heavy hydrogen isotopes, *Adv. Space Res.*, *41*, 86–91.

Looper, M. D., J. B. Blake, J. R. Cummings, and R. A. Mewaldt (1996), SAMPEX observations of energetic hydrogen isotopes in the inner zone, *Radiat. Meas.*, *26*(6), 967–978.

Looper, M. D., J. B. Blake, and R. A. Mewaldt (1998), Maps of hydrogen isotopes at low altitudes in the inner zone from SAMPEX observations, *Adv. Space Res.*, *21*(12), 1679–1682.

Lorentzen, K. R., J. E. Mazur, M. D. Looper, J. F. Fennell, and J. B. Blake (2002), Multisatellite observations of MeV ion injections during storms, *J. Geophys. Res.*, *107*(A9), 1231, doi:10.1029/2001JA000276.

Mazur, J. E., J. B. Blake, P. L. Slocum, and M. K. Hudson (2006), The creation of new ion radiation belts associated with solar energetic particle events and interplanetary shocks, in *Solar Eruptions and Energetic Particles*, *AGU Geophys. Monogr. Ser.*, vol. 165, edited by N. Gopalswamy, R. Mewaldt, and J. Torsti, pp. 345–352.

Mewaldt, R. A., C. M. S. Cohen, A. W. Labrador, R. A. Leske, G. M. Mason, M. I. Desai, M. D. Looper, J. E. Mazur, R. S. Selesnick, and D. K. Haggerty (2005), Proton, helium, and electron spectra during the large solar particle events of October–November 2003, *J. Geophys. Res.*, *110*, A09S18, doi:10.1029/2005JA011038.

Moskalenko, I. V., and S. G. Mashnik (2003), Evaluation of production cross sections of Li, Be, B in CR, *Proc. 28th Int. Cosmic Ray Conf.*, 1969–1972.

Picozza, P., et al. (2007), PAMELA—A payload for antimatter matter exploration and light-nuclei astrophysics, *Astropart. Phys.*, *27*, 296–315.

Phillips, G. W., et al. (2001), Correlation of upper-atmospheric ^{7}Be with solar energetic particle events, *Geophys. Res. Lett.*, *28*(5), 939–942.

Pugacheva, G. I., W. N. Spjeldvik, A. A. Gusev, I. M. Martin, and N. M. Sobolevsky (1998), Hydrogen and helium isotope inner radiation belts in the Earth's magnetosphere, *Ann. Geophys.*, *16*, 931–939.

Ramaty, R., and R. E. Lingenfelter (1969), Cosmic-ray deuterium and helium-3 of secondary origin and the residual modulation of cosmic rays, *Astrophys. J.*, *155*, 587–608.

Selesnick, R. S. (2001), Simulation of the anomalous cosmic ray radiation belt with atmospheric production and decay, *Geophys. Res. Lett.*, *28*(17), 3417–3420.

Selesnick, R. S., and R. A. Mewaldt (1996), Atmospheric production of radiation belt light isotopes, *J. Geophys. Res.*, *101*(A9), 19,745–19,757.

Selesnick, R. S., A. C. Cummings, J. R. Cummings, R. A. Mewaldt, E. C. Stone, and T. T. von Rosenvinge (1995), Geomagnetically trapped anomalous cosmic rays, *J. Geophys. Res.*, *100*(A6), 9503–9518.

Selesnick, R. S., M. D. Looper, and R. A. Mewaldt (2007a), A theoretical model of the inner proton radiation belt, *Space Weather*, *5*, S04003, doi:10.1029/2006SW000275.

Selesnick, R. S., M. D. Looper, R. A. Mewaldt, and A. W. Labrador (2007b), Geomagnetically trapped antiprotons, *Geophys. Res. Lett.*, *34*, L20104, doi:10.1029/2007GL031475.

Sibeck, D. G., B. H. Mauk, J. M. Grebowsky, and N. J. Fox (2006), The living with a star Radiation Belt Storm Probes mission and related missions of opportunity, *Eos Trans. AGU*, *87*(52), Fall Meet. Suppl., Abstract SM33A-0330.

Solanki, S. K., I. G. Usoskin, B. Kromer, M. Schussler, and J. Beer (2004), Unusual activity of the Sun during recent decades compared to the previous 11000 years, *Nature*, *431*, 1084–1087, doi:10.1038/nature02995.

Tripathi, R. K., F. A. Cucinotta, and J. W. Wilson (1999), Universal parameterization of absorption cross sections: Light systems, *NASA/TP_1999_209726*.

Wefel, J. P., J. Chen, J. F. Cooper, T. G. Guzik, and K. R. Pyle (1995), The isotopic composition of geomagnetically trapped helium, *Proc. 24th Int. Cosmic Ray Conf.*, *4*, 1021–1024.

M. D. Looper, Aerospace Corporation, P.O. Box 92957-M2/260, Los Angeles, CA 90009-2957, USA. (mark.d.looper@aero.org)

R. A. Mewaldt, Physics Department, California Institute of Technology, MC 220-47, Pasadena, CA 91125, USA. (rmewaldt@srl.caltech.edu)

R. S. Selesnick, P.O. Box 515381 #6702, Los Angeles, CA 90051-6681, USA. (rselesnick@gmail.com)